# Nano-positioning and tubulin conformation contribute to axonal transport regulation of mitochondria along microtubules

Peer-reviewed author version

Van Steenbergen, Valerie; Lavoie-Cardinal, Flavie; Kazwiny, Youcef; Decet, Marianna; Martens , Tobie; Verstreken, Patrik; BOESMANS, Werend; De Koninck, Paul & Vanden Berghe, Pieter (2022) Nano-positioning and tubulin conformation contribute to axonal transport regulation of mitochondria along microtubules. In: PROCEEDINGS OF THE NATIONAL ACADEMY OF SCIENCES OF THE UNITED STATES OF AMERICA, 119 (45) (Art N° e2203499119).

DOI: 10.1073/pnas.2203499119
Handle: http://hdl.handle.net/1942/39370

PNAS

# Main Manuscript for

## Nano-positioning and tubulin conformation contribute to axonal transport regulation of mitochondria along microtubules

Valérie Van Steenbergen1,7, Flavie Lavoie-Cardinal2, Youcef Kazwiny1, Marianna Decet5, 6, 7, Tobie Martens1, Patrik Verstreken5, 6, 7, Werend Boesmans1,3,4, Paul De Koninck2, Pieter Vanden Berghe1,7*

Affiliations:

1 Laboratory for Enteric Neuroscience, Department of Chronic Diseases, Metabolism and Ageing, KU Leuven, Leuven, Belgium.

2 CERVO Brain Research Center, Université Laval, Québec, Canada.

3 Department of Pathology, GROW-School for Oncology and Developmental Biology, Maastricht University Medical Center, Maastricht, The Netherlands.

4 Biomedical Research Institute (BIOMED), Hasselt University, Hasselt, Belgium.

5 VIB-KU Leuven Center for Brain & Disease Research, Leuven, Belgium,

6 Department of Neurosciences, KU Leuven, Leuven, Belgium,

7 Leuven Brain Institute, KU Leuven, 3000 Leuven, Belgium.

*Corresponding author

**Email:** pieter.vandenberghe@kuleuven.be

ORCID:

VVS: 0000-0002-5836-2122; FLC: 0000-0002-4496-5088; YK: 0000-0002-6284-225X; MD: -; TM: -; PV: 0000-0002-5073-5393; WB: 0000-0002-2426-0451; PDK: 0000-0002-6436-1062; PVB: 0000-0002-0009-2094

**Author Contributions:** Methodology: VVS, PVB. Investigation: VVS, FLC, YK, MD, TM. Data discussion: VVS, WB, PV, PVB. Writing – Original draft: VVS. Writing – Review & Editing: VVS, FLC, YK, MD, TM, PV, WB, PDK, PVB. Conceptualization: VVS, PVB. Funding: PV, PDK, PVB.

**Competing Interest Statement:** : The authors declare that no competing interests exist.

**Classification:** Biological Sciences - Neuroscience

**Keywords:** Microtubules, Mitochondria, Transport, Neurobiology, Tubulin, Axon

**This PDF file includes:**

Main Text

Figures 1 to 5

**Abstract**

Correct spatiotemporal distribution of organelles and vesicles is crucial for healthy cell functioning and is regulated by intracellular transport mechanisms. Controlled transport of bulky mitochondria is especially important in polarized cells such as neurons that rely on these organelles to locally produce energy and buffer calcium. Mitochondrial transport requires and depends on microtubules that fill much of the available axonal space. How mitochondrial transport is affected by their position within the microtubule bundles is not known. Here, we found that anterograde transport, driven by kinesin motors, is susceptible to the molecular conformation of tubulin in neurons both *in vitro* and *in vivo*. Anterograde velocities negatively correlate with the density of elongated tubulin dimers like GTP-tubulin. The impact of the tubulin conformation depends primarily on where a mitochondrion is positioned, either within or at the rim of microtubule bundle. Increasing elongated tubulin levels lowers the number of motile anterograde mitochondria within the microtubule bundle and increases anterograde transport speed at the microtubule bundle rim. We demonstrate that the increased kinesin velocity and density on microtubules consisting of elongated dimers add to the increased mitochondrial dynamics. Our work indicates that the molecular conformation of tubulin contributes to the regulation of mitochondrial motility and as such to the local distribution of mitochondria along axons.

## Significance statement

Transport patterns of mitochondria are diverse with changes in velocity, directions and pauses. Previous studies have mainly aimed at unraveling how motor proteins and their calcium dependency direct transport but fall short to elucidate all transport patterns. Here, we report that tubulin conformation, highly dependent on GTP hydrolysis, regulates mitochondrial transport. On the one hand GDP- or GTP- bound tubulin alters the straightness of the microtubule bundles, influencing transport especially when cargo is positioned within the microtubule bundle. On the other hand, the GTP-bound conformation facilitates kinesin-driven transport at the rim of the microtubule bundle. Microtubules are therefore not merely a passive player for mitochondrial transport as tubulin can directly regulate mitochondrial transport.

## Main Text

## Introduction

Mitochondria are found in almost all eukaryotic cell types and are of key importance to maintain intracellular processes such as adenosine triphosphate (ATP) production, calcium homeostasis, stress responses and cell fate (1-3). As mitochondria are formed in the cell soma, active transport towards sites with a high energy demand is required for healthy cellular function. The long, narrow and highly branched axonal and dendritic projections of nerve cells present an extra challenge for transport of these organelles to their target sites and require precise spatiotemporal regulation of the transport machinery (4-7). Inefficient organization of the molecular machinery can lead to mitochondrial transport deficits, which are implicated in neurodegenerative diseases such as Amyotrophic lateral sclerosis (ALS), Alzheimer's and Huntington's disease (8-10).

The molecular railroads used for long-distance intracellular transport are microtubules, long tubulin polymers that provide binding sites for kinesin and dynein motor proteins (11). Upon polymerization, tubulin dimers bind in an exchangeable manner to guanosine triphosphate (GTP) at the ß-tubulin subunit, favoring a stable, elongated dimer conformation. Once incorporated in the tubular lattice, GTP hydrolysis leads to a conformational change towards a less stable and compacted guanosine diphosphate (GDP)-bound tubulin dimer. Because GTP hydrolysis lags behind microtubule growth, it was thought that these stable GTP-tubulin dimers were only present at the microtubule growing tip to prevent depolymerization (12-14). However, recent studies indicate that GTP-bound tubulin dimers are also present further along the microtubule lattice (15-17). These so-called GTP-tubulin islands could serve as rescue sites to prevent depolymerization of the microtubule or provide a location for self-repair (16, 18-21).

While it is likely that a high GTP- to GDP-tubulin ratio is mainly required to strengthen the complex architecture in neuronal projections, it also influences binding of kinesin motor proteins. As these motors have been shown to regulate sorting of cargo to the somatodendritic and axonal domains, the presence of GTP-bound tubulin dimers could, apart from influencing general intracellular transport, also be involved in regulating polarized transport (17, 22, 23). How kinesin binding affinity is regulated by the conformation of tubulin depends on the kinesin subtype. KIF1S binds more weakly to GTP-bound than to GDP-bound tubulin dimers while KIF5 has increased binding affinity to GTP-bound tubulin dimers (17, 24, 25). Moreover, the processive motion of kinesin motors depends on the conformational state of the tubulin dimer, whereby the GTP-bound conformation enables kinesin to move faster on *in vitro* polymerized microtubules (26). T. Shima *et al.* have shown that KIF5C not only preferentially binds GTP-bound tubulin dimers but that it can even pull the conformational state of tubulin from a GDP- to a GTP-like state (25). However, these findings conflict with effects of drugs that interfere with conformational changes in tubulin dimers such as taxol, a commonly used chemotherapeutic drug. Taxol blocks spindle formation and thus cell division by locking new GTP-bound tubulin dimers in their elongated conformation, resisting lattice compaction induced by GTP hydrolysis (27-30). As taxol raises the amount of stable and elongated tubulin dimers, increased kinesin binding and thus more efficient anterograde transport is expected. However, a conundrum arises as one of taxol's common side effects is rather an interruption of axonal transport, possibly

leading to chemotherapy induced peripheral neuropathy (CIPN) (31-33). Thus, how the conformational state of tubulin regulates organelle transport is poorly understood.

In this study, we elucidate how changes in the tubulin dimer conformation locally regulate mitochondrial transport. We show that the presence of elongated tubulin dimers halts anterograde transport specifically of the mitochondria located inside the microtubule bundle, without hindering mitochondrial transport that occurs along the rim of the microtubule bundle. On the contrary, we show that this remaining motile fraction is transported faster possibly due to increased processive motion of KIF5B, a kinesin motor for mitochondria that preferentially binds tubulin in its elongated conformation. Finally, using *Drosophila melanogaster* as a model, we show that increasing the elongated tubulin dimer conformation *in vivo* also leads to a reduction in mitochondrial transport in the anterograde direction while transport velocities of the remaining motile fraction are increased.

## Results

### The conformation of tubulin influences mitochondrial transport patterns

Mitochondrial transport is tightly regulated by several players such as motor proteins, intracellular calcium levels and tubulin posttranslational modifications. We set out to determine whether the conformation of the microtubule tracks has a role in regulating axonal transport of mitochondria. To this end, we first characterized the distribution of GTP- and GDP-bound tubulin dimer ratios in axonal and dendritic projections of hippocampal neurons (Fig. 1A). A general α-tubulin antibody was used to label all microtubules in combination with an antibody that recognizes specific tubulin dimers in a GTP-bound conformation (15). Dendritic and axonal processes were identified by immunohistochemistry (Fig. 1A). Even though dendritic processes contain more microtubules, we clearly show that the relative GTP-bound tubulin content is higher in axons (Fig. 1B), confirming the immunoelectron microscopy data published by Nakata et al. (17). Next, we combined live mitochondrial transport recordings with a post-hoc immunohistochemical staining to correlate mitochondrial transport parameters (Fig. 1C,D), with GTP-tubulin density in all neuronal processes. Interestingly, despite the complexity of mitochondrial transport regulation and the multiple intracellular processes involved, we were able to detect a mild but highly significant negative correlation between GTP-tubulin density and anterograde, but not retrograde, transport velocity (Fig. 1E). The correlation of GTP-tubulin content with anterograde transport prompts the hypothesis that the conformation of tubulin might indeed affect mitochondrial transport efficacy. To investigate whether molecular changes in the tubulin dimer could alter mitochondrial transport, taxol was used to increase the amount of elongated tubulin dimers (Fig. 1F). We opted for a low dose of taxol (10 nM), sufficient to raise the amount of elongated tubulin dimers, while ensuring that there is no increase in overall microtubule mass (supplementary figure 1A) as we and others have shown previously (34, 35). We chose to restrict our analysis to axons only, as to correctly assess antero- versus retrograde transport, controlled by kinesin and dynein motors respectively. Treatment with taxol revealed a specific effect on anterograde kinesin-based transport as the number of anterograde but not retrograde motile mitochondria was significantly reduced (Fig. 1G). Furthermore, while the amount of tubulin dimers in a GTP-bound conformation negatively correlates with average anterograde transport velocity in control cells (Fig. 1E), increasing the amount of elongated tubulin dimers beyond physiological levels with taxol leads to an increase in anterograde velocity of the few mitochondria that are still motile (Fig. 1H). To address the possibility that taxol had direct effects on mitochondrion shape and functionality, which might affect mitochondrial transport in a microtubule independent way, we analyzed mitochondrial shape in relation to transport parameters. While mitochondria (stationary and moving ones) in taxol-treated axons were overall smaller in size (Supplementary figure 2A), we found no large changes in morphology of anterograde motile mitochondria nor a correlation between distinct shape parameters and their respective velocity (Supplementary figure 2B). To further assess mitochondrial functionality, we performed an electron flow assay on isolated mitochondria of mouse brain tissue incubated with taxol or DMSO and observed no significant changes in respiratory complex activity both groups (Supplementary figure 2C). We therefore conclude that the observed transport changes are not related to direct taxol-induced mitochondrial dysfunction. Similar to taxol, an epothilone B (4h, 10 nM) treatment significantly reduced

the number of anterograde but not retrograde motile mitochondria while increasing the velocity of the remaining motile fraction of anterograde but not retrograde mitochondria (Supplementary figure 3). Taken together, these experiments show that the conformation of tubulin, related to the molecular changes upon GTP or GDP binding, could be a regulator of mitochondrial transport patterns.

**Mitochondria are transported along and within the microtubule bundle**

*In vitro* work (36) has shown that the elongated conformation of tubulin renders microtubules more straight and less flexible when polymerized in cell free situations. Building on this information, straight microtubules in an otherwise wandering axon, might impede axonal mitochondria to move, especially when being transported within the microtubule bundle, rather than at the rim where the plasma membrane seems more likely to bulge upon passing of large organelles (Supplementary figure 4). Therefore, the straightness of microtubules would only hinder transport if mitochondria are also transported within the microtubule bundle rather than at the rim. This hypothesis, if true, would explain the negative correlation between the physiological GTP-GDP tubulin ratio and anterograde velocities (Fig. 1E). With GTP-GDP tubulin ratio's beyond physiological levels, the excessive increase in microtubule straightness could not only slow down transport but even halt mitochondrial transport, such as seen in several taxol-treated axons (Fig. 1F,G).

The exact nano-positioning of mitochondria during axonal transport is however not known. Live 2D STED microscopy time-lapse recordings of mitochondria and microtubules (Supplementary Figure 5, Supplementary Movie 1) reveal a subset of motile mitochondria indeed being transported at the rim of the microtubule bundle (Fig. 2A), while others appear to be within the bundle. Even though 2D STED has sufficient resolution to resolve the position of a mitochondrion in XY it does lack Z-resolution (along the imaging axis). To accurately assess their position in Z, we used 3D STED (see methods) in fixed preparations as the time to acquire these image stacks as well as the optical STED powers needed are not compatible with live imaging. To ensure that we were analyzing mitochondria, while they were transported, we acutely added paraformaldehyde at the time transport of mitochondria was detected in a specific axonal segment. This allowed identifying motile and stationary mitochondria during post-hoc immunohistochemistry (Fig. 2B, Supplementary Figure 5). We proceeded with 3D-STED microscopy on these fixed samples which enabled full 3D characterization of the mitochondrial localization relative to the microtubule network (Fig. 2C-F). The percentage of the optical surface overlap of microtubules per mitochondrion, hereinafter referred to as a surface$^{MITO-MT}$ overlap, was calculated as a measure for mitochondrial confinement within the microtubule bundle. The median surface$^{MITO-MT}$ overlap of the motile mitochondria was 52.4%, indicating that a significant proportion of mitochondria are surrounded by microtubules as they are transported (Fig. 2F-H). As mitochondria are not only transported at the rim but also within the microtubule bundle, changing the straightness of microtubules by altering the tubulin conformation has indeed an impact on mitochondrial transport.

**Increasing microtubule straightness hinders mitochondrial transport within the microtubule bundle**

We hypothesized that the loss of motile mitochondria is mainly due to steric hindrance owing to the elongated dimer conformation as induced by taxol. Therefore, only mitochondria transported between the microtubules would become immotile while mitochondria at the rim are still transported after taxol treatment. To test this, we compared axonal transport in hippocampal cultures incubated either with taxol or DMSO (Fig. 3A, B). Cells were fixed on stage concurrent with detection of mitochondrial motility in the anterograde direction as shown previously (Supplementary Figure 5). Using 3D STED microscopy on the fixed samples, no significant difference was detected in surface$^{MITO\text{-}MT}$ overlap when all mitochondria (both motile and stationary) were compared between control and taxol-treated samples (Fig. 3C). However, when only the motile fraction was considered, the surface$^{MITO\text{-}MT}$ overlap was significantly lower in taxol-treated cells (Fig. 3D), indicating that these mitochondria were positioned at the rim. To test whether mitochondria at the rim, would be faster by default, we correlated the surface$^{MITO\text{-}MT}$ overlap with anterograde velocity in control cells to exclude that the observed increased transport velocity in the taxol condition does not arise from an outer-rim transport selection bias (Supplementary figure 6). Moreover, taxol did not have any direct effect microtubule bundle thickness nor its correlation with anterograde velocities (Supplementary figure 6). The reduction in the amount of transport after taxol thus mainly arises from halting those mitochondria transported within the microtubule bundle but not of those at the rim, as illustrated in Figure 3E.

**Kif5B velocity and density are increased along elongated tubulin dimers**

While the nano-position of the mitochondrion during transport can explain the reduction in anterograde motile mitochondria upon taxol treatment, it does not explain why the remaining motile fraction is transported at increased velocities (Fig. 1H). As with taxol treatment, mitochondria are mainly motile at the outer rim rather than within the microtubule bundle, it could be possible that motile mitochondria at the rim in general are transported at increased velocities compared to these within the bundle. We however found no correlation between mitochondrial velocity and colocalization percentage in control cells (Supplementary figure 6A, gray), indicating that the location of the mitochondrion does not determine its velocity under physiological GTP/GDP-tubulin levels. Previously published data utilizing *in vitro* polymerized microtubules has shown that the conformation of tubulin also affects kinetics and binding of motor proteins such as kinesin (17, 26), however it remains unknown whether this is also valid in living cells such as neurons. We first investigated KIF5B kinetics on distinct molecular tubulin conformations. Neurons expressing Kif5b-GFP were imaged using total internal reflection (TIRF) microscopy (Fig. 4B and Supplementary Figure 7). We found that kinesin motors move significantly faster in taxol-treated cells (Fig. 4B). Apart from altered kinetics of kinesin motors, KIF5 motors have previously been shown to preferentially bind GTP-tubulin rich microtubules (17). To test whether also binding of kinesin is altered, we used multicolor STED microscopy to ensure sufficient resolution to detect and assess KIF5b motor proteins on the mitochondrion's surface (Fig. 4C, 4D, Supplementary Figure 8). We first restricted the quantification of KIF5B motors to those that optically overlapped with the mitochondrial surface. Even though this does not prove binding, it is highly likely that those

KIF5B's bound to mitochondria at the time of fixation were included. The relative number of kinesin motors per surface area (Fig. 4E) was not different between control and taxol-treated cells. To further refine the analysis, we restricted the KIF5B inclusion to those that optically overlapped, not only with the mitochondria, but specifically with the MITO-MT surface. Although this spatial confinement does not prove that all KIF5B are bound, it does ensure the inclusion of all active motors bound both to MT and cargo during transport. Interestingly, significantly more motors were present within this selection in the taxol-treated condition (Fig. 4F), suggesting that the density of kinesin motors along microtubules and in proximity to mitochondria is higher. Finally, we aimed at elucidating whether this increased kinesin density, and thus likelihood of functional kinesin binding, also affects anterograde velocity. We used an optogenetic technique to optically control kinesin binding onto mitochondria (Fig. 4G) (37). As seen in the kymographs presented in Fig. 4H, illumination (yellow dashed line), forces anterograde transport in axonal processes. Upon illumination and forced binding to kinesin the number of transported mitochondria rose ~2.5 fold in both control and taxol conditions. However, the relative effect of taxol on the number of transported mitochondria remained also in the light induced condition (Fig 4J). Interestingly, the difference in anterograde velocity between control and taxol, disappears when kinesins are optically forced to bind cargo, since optogenetic activation increases the velocity in the control condition (Fig 4 J) to that in taxol, without affecting the latter (Fig 4 J taxol).

Taken together, these data are in line with a model in which there is sterical hindrance induced by the taxol treatment: forced binding of kinesin motors to mitochondria increases the number of motile mitochondria, but cannot cancel out the effect of hindrance (Fig 4J). While on the other hand, anterograde transport velocities are no longer significantly different between control and taxol cells after forced binding since only velocities in control cells are increased. Forced binding of motor proteins in control cells therefore mimics the effect of taxol incubation with respect to anterograde velocities. The higher velocity of kinesin motors along elongated tubulin dimers and their abundant presence at the microtubule-mitochondrial interface provide a means to explain the observed increased anterograde velocities.

**Taxol halts the majority of mitochondrial transport in the anterograde direction while increasing anterograde transport velocities *in vivo***

Finally, we tested whether the conformation of tubulin dimers also regulates mitochondrial transport *in vivo*. *Drosophila melanogaster* with neuronal TdTomato-tagged mitochondria were put on starvation for 3 hours followed by feeding on regular food supplemented with DMSO or 100 nM taxol within 8 hours from eclosion (Figure 5A). Taxol can reach the nervous system of these flies through both oral drug administration as well as peripheral contact with taxol as flies were able to move freely in their container with food. After 24 and 48 hours of continuous taxol administration, flies were mounted in glass chambers and mitochondrial transport was recorded in the neuronal projections adjacent to vein L2 in the wing (Figure 5B-D). The taxol concentration was chosen based on a pilot experiment (Supplementary Figure 9) that assessed taxol intake and relevant changes in mitochondrial transport parameters using increasing taxol concentrations. We found a significant decrease in anterograde mitochondrial motility after 24 and 48 hours of continuous taxol administration, while retrograde

transport was only significantly reduced after 48 hours (Figure 5E). Anterograde transport velocities were significantly increased after 24 and 48 hours taxol while retrograde transport velocities remained unchanged (Figure 5F). Thus, changing the tubulin dimer conformation regulates anterograde mitochondrial transport *in vivo* in a similar manner.

## Discussion

The central nervous system has a high-energy need and proper spatial and temporal distribution of mitochondria to produce local energy, are crucial (8, 38, 39). Failure to transport mitochondria has been linked to several neurodegenerative diseases including Parkinson's disease, Alzheimer's disease and Amyotrophic Lateral Sclerosis (8, 40, 41), which boosted studies on mitochondrial transport mechanisms. Apart from the identification of distinct motor protein families, also unraveling regulatory proteins such as the Miro-Milton complex and its calcium dependency has been key for understanding transport in neurons (42-45). Moreover, changes at the level of the tubulin dimer can also influence intracellular transport as the nucleotide (GTP/GDP) bound to the tubulin dimer determines its conformation (28, 36) and consequently affects motor protein activity (17, 25, 26, 46). Drugs interfering with tubulin conformations such as taxol, a drug that favors GTP-tubulin and locks it in its elongated conformational state (15, 27-29, 36, 47), have also been shown to disrupt transport dynamics (31-33). However, exactly how transport is affected upon changes in the conformational state of the tubulin dimer is not fully understood. Here, we describe how the tubulin dimer conformation regulates mitochondrial transport dynamics and how that is affected by mitochondrial positioning along the microtubules.

We first set out to understand whether the presence of GTP and GDP tubulin dimers along the microtubule lattice could regulate organelle transport. In agreement with previous research, we show that axonal projections have a higher GTP-tubulin density as compared to dendrites (17). Furthermore, a negative correlation between GTP-tubulin density and anterograde transport velocities indicates a possible relationship between tubulin conformations and transport dynamics. Upon binding of drugs that increase the amount of elongated tubulin dimers (taxol and epothilone B), the number of anterograde motile mitochondria was significantly reduced while no change in the number of retrograde motile mitochondria was detected. This could be linked to the fact that kinesin motors bound to cargo have more difficulty traversing obstacles owing to their limited step-size and short neck-linker as compared to dynein motors (48-51). Increasing the amount of stable, elongated tubulin dimers also led to increased anterograde- but without affecting retrograde velocities. This is in line with the direction-dependent decrease in motile mitochondria and indicates that processivity of specifically kinesin motors depends on the conformational changes in tubulin dimers.

The negative correlation between anterograde transport velocities and elongated tubulin density in control cells and the reduction of motile anterograde mitochondria in taxol-treated cells could be explained by steric hindrance. Indeed, it has previously been shown using *in vitro* polymerized microtubules that taxol increases the straightness of microtubules (36). We first showed that mitochondria are also being transported between these (straight) microtubules and not solely at the rim. Upon incubation with taxol however, the pool of motile mitochondria within the microtubule bundle

but not at the rim become stationary. The straightness of the microtubule network, influenced by tubulin conformations, can thus indeed regulate mitochondrial transport. The overall organization of the microtubule network has furthermore proven to be important to regulate lysosomal transport. Balint et al. (52) have shown that lysosomes pause at microtubule intersections, especially when the inter-microtubule space is below 100 nm. This further indicates that microtubule flexibility is required to facilitate transport of cargo between bundles. The significant decrease in mitochondrial size, particularly in the stationary state (as no difference in motile state, Suppl. Fig 2), coupled with fewer numbers of moving mitochondria after taxol treatment may also suggest that mitochondria, depending on their size, may be impeded in gaining access and/or docking to the inner portions of the tubulin fiber tracts. This could also serve to "filter" or "sieve" cargo and affect the amount and nature of cargo being transported.

To elucidate why mitochondria at the rim of taxol-treated neurons move at increased velocities, we focused on kinesin motors and their interaction with distinct molecular tubulin conformations. We first show that kinesin motors move faster on taxol-treated microtubules, which aligns with results reported using *in vitro* polymerized microtubules (26). While most studies using *in vitro* polymerized microtubules agree with our findings in neuronal cultures, some studies concerning kinesin-1 binding affinity and velocity report no significant difference between microtubules consisting of the elongated – or compacted tubulin conformation (53, 54). It should be noted that the latter studies compared similar conformational states of the tubulin dimer, i.e. microtubules polymerized with GMPCPP, a very slowly hydrolysable GTP analog, and taxol-stabilized microtubules. While these studies indicate the importance of stabilization methods for *in vitro* polymerized microtubule assays, they also provide further evidence of the conformational similarities between taxol-bound tubulin dimers and native GTP-bound tubulin as no kinesin-dependent differences between both microtubule populations were reported.

Apart from kinetic properties of kinesin motors, we also explored the possibility that conformational changes in tubulin could influence kinesin density along the microtubule lattice. We found a significant increase in the amount of kinesin motors located on the surface overlap of specifically motile mitochondria and taxol-treated microtubules, in line with a previous study by Nakata *et al*. (17). The abundancy of kinesin motors increases the probability that they are functionally bound to the mitochondria, however, we cannot be certain that the density of kinesin motors at this interface also leads to increased mitochondrial velocities. To this end, we employed optogenetic tools to force binding of kinesin motors to mitochondria. We found that upon activation of the optogenetic construct, the number of motile mitochondria remained significantly reduced in the taxol-treated condition. This indicates and strengthens our conclusion that a large fraction of the stationary pool of mitochondria after taxol treatment are sterically hindered to be transported within the straight microtubule bundle as merely increasing kinesin binding cannot overcome this hindrance. On the other hand, forced binding of kinesin motors to mitochondria led to similar anterograde velocities between control and taxol treated cells, owing to increased velocities in control cells upon optogenetic activation. These results indicate that increasing kinesin binding results in similar, possibly maximal, anterograde transport velocities as seen in the small fraction that was still motile and fast in taxol conditions. We therefore

conclude that the cause of faster anterograde transport velocities in taxol could be two-fold, on the one hand the processive motion of kinesin motors is more efficient, resulting in increased motor protein velocities, while on the other hand an increased density of kinesin motors at the microtubule-mitochondrial interface could facilitate binding which results in faster velocities.

Finally, we confirmed that tubulin conformations are also relevant in regulating mitochondrial transport *in vivo*. To change the molecular conformation of tubulin dimers, we fed adult *Drosophila melanogaster* taxol. Previous studies using oral administration of taxol in fruit flies are limited to larvae and use high concentrations that lead to neuronal degeneration (55, 56). As we were mainly interested in early effects of taxol, preceding axonal degeneration, we first performed a pilot study using various low taxol concentrations. From the bell-shaped dose-velocity curve, we opted for 100 nM taxol for oral administration to ensure enough taxol is taken up while reducing possible adverse secondary effects linked to axonal degeneration. We found that taxol reduced anterograde motility both after 24 and 48 hours, while retrograde transport was decreased only after 48 hours, possibly a consequence of fewer mitochondria being present due to early onset reduced anterograde transport. We also note that mitochondrial transport in control flies decreased during maturation as shown previously (57). Furthermore, anterograde transport velocities are significantly increased after taxol administration for both timepoints while retrograde transport velocities remain unchanged.

In summary, we show that the molecular conformation of the tubulin dimer influences mitochondrial transport in two distinct ways depending on mitochondrial localization. On one hand, the increased straightness of microtubules enriched in elongated tubulin hinders specifically those mitochondria travelling within the microtubule bundle, possibly explaining why studies investigating CIPN linked to taxol treatment observe a decrease in motile organelles and vesicles (31-33, 58) . On the other hand, mitochondria mobile at the rim of the microtubule bundle are transported at increased velocities as the molecular conformation of tubulin affects kinesin binding and processive velocity in neuronal projections. As an increased density of elongated dimers leads to straighter microtubules, it is conceivable that processive motion of kinesin motors is mechanically more efficient, resulting in increased transport speed. While taxol is known to alter the conformation of the tubulin dimer, we cannot exclude the possibility that this conformation change further leads to additional cascade of posttranslational modifications of tubulin or binding of MAPs, which in turn could also affect intracellular transport. We therefore conclude that the conformation of tubulin dimers within the microtubule lattice is an important regulator of intracellular transport, either direct or indirect, and that the specific location of motile mitochondria is crucial for the regulatory effect in neurons both *in vitro* and *in vivo*. These findings are relevant not only to understand intracellular transport mechanisms but are also crucial for cancer research and more specifically how chemotherapeutic agents can interfere with neuronal processes such as intracellular transport.

## Materials and methods

### Primary neuronal cultures

All procedures were approved by the Animal Ethics Committee of the University of Leuven (Belgium) and Université Laval (Canada). All cell cultures apart from these used for live STED imaging were derived from mouse hippocampal tissue. Postnatal day 0-5 C57Bl/6J mouse pups were quickly decapitated before dissection. Hippocampi were dissected in sylgard dishes containing cold sterile Hank's Buffered Salt Solution (HBSS in mM: 5.33 KCl, 0.44 $KH_2PO_4$, 137.93 NaCl, 0.34$Na_2HPO_4.7H_2O$, 5.56 D-glucose and 10 HEPES). The tissue was minced and incubated in 0.25% trypsin-EDTA (Gibco) supplemented with 80 U/ml DNAse (Roche) for 10 min at 37°C. After three consecutive wash steps with HBSS supplemented with 10% fetal bovine serum (FBS, Sigma Aldrich), the tissue was mechanically dissociated by trituration with syringes with decreasing diameter. Cells were plated at 5 x $10^5$ cells per coverslip (18 mm diameter, coated with poly-D-Lysine) and grown in a 37°C, 5% $CO_2$ incubator in Neurobasal-A media (Thermo Fisher Scientific) supplemented with 0.5% penicillin / streptomycin (Lonza), 0.5% B27 (Gibco), 100 ng/ml nerve growth factor (Alomone Labs) and 2mM Glutamax (Thermo Fisher Scientific). Media was replaced 1:1 every three days and cells were used at 7 DIV unless stated otherwise. For live STED recordings, rat hippocampal neurons were prepared as described previously (59).

### Transfection

After 6 DIV, expression of TOM20-mCherry-LOVpep and Kif5b-GFP-ePDZb1 (gift from L.C. Kapitein (37)) was induced in neuronal cultures to guide anterograde transport in axons upon light-induced heterodimerization. Per well, 0.5 µg plasmid was mixed with 0.02% Lipofectamine 2000 reagent (Invitrogen) in Neurobasal-A media and incubated at room temperature for 30 min. The mixture was added dropwise to the wells and media were replaced after 4 hours. Expression was verified the following day.

### Pharmacological treatment

Taxol- and epothilone B-treated cultures were incubated with 10 nM taxol or 10 nM epothilone B dissolved in DMSO (4 h) in plating medium. Control cultures were treated with an equal amount of DMSO (0.1 %). During imaging, plating medium with DMSO, taxol or epothilone B was replaced by HEPES buffer (in mM: 148 NaCl, 5 KCl, 1 $MgCl_2$, 10 Glucose, 10 HEPES, 2 $CaCl_2$).

### Mitochondrial transport imaging & analysis

B27 media was replaced by HEPES buffer (in mM: 148 NaCl, 5 KCl, 1 $MgCl_2$, 10 Glucose, 10 HEPES, 2 $CaCl_2$) for live cell imaging at 37°C. A Zeiss LSM 780 confocal laser scanning microscope (Zeiss) fitted with an Argon laser (488 nm) and solid state lasers (561, 633 nm) was used for mitochondrial imaging (Mitotracker red, 75 nM, 10 min incubation, Thermo Fisher Scientific) in combination with an

LD LCI Plan-Apochromat 25x/0.8 Imm Corr DIC M27 water-immersion objective. In-house Igor pro (Wavemetrics, OR, USA) code was used to generate kymographs and analyze mitochondrial transport time lapse recordings as described previously (35). Mitochondrial tracks were marked in the kymographs, and general transport parameters per mitochondrion, such as overall velocity, instantaneous velocity, transport periods, pauses, direction changes… were extracted from these kymographs (Suppl. table 1). For velocity measurements that were made in relation to the surface overlap percentage, only the final motile segment, without direction changes and pauses, was included, and thus this velocity represents the instantaneous transport velocity at the time paraformaldehyde was added to acutely stop neuronal function. Mitochondrial transport was analyzed at similar distances from the cell soma (Table 2) in axons that were identified process length and diameter.

**Electron flow assay isolated mitochondria**

Mitochondria were isolated from hippocampal brain tissue using the microTOM22 beads technology (Miltenyi Biotec). The mouse mitochondrial extraction and isolation kit were used for tissue homogenization, digestion and mitochondrial isolation. The isolated mitochondria were then incubated with either taxol in DMSO (10 nM, 1 h) or an equal amount of DMSO as control. These mitochondria were used for the electron flow assay according to the company's protocol (Agilent Seahorse). In short, mitochondria were resuspended in 9:1 MAS-MSHE buffer and 2 µg mitochondrial protein was plated. The following toxins and substrates were dissolved in MAS buffer before injection: 20 µM rotenone, 100 mM succinate, 40 µM antimycin A and 100 mM ascorbate with 1mM TMPD. Injection volumes were adjusted to ensure a 10 times dilution as a final concentration.

**Immunofluorescence labeling**

Cells were fixed with 4% paraformaldehyde (PFA, 30 min, RT) and washed in phosphate buffered saline (PBS). After fixation, cells were incubated in blocking medium containing PBS, 4% serum from secondary hosts (Chemicon International) and 0.1% Triton X-100 (Sigma) (2 h, RT), followed by overnight incubation at 4°C with several primary antibody combinations. Primary antibodies used were: goat TAU (1:1000, cat. number SC1995, Santa Cruz Biotechnology), chicken MAP2 (1:5000, cat. number ab5392, Abcam), rabbit α-tubulin (1:1000, cat. number ab18251, Abcam), rat α-tubulin (1:50, cat. number MA180189, Invitrogen), chicken beta III tubulin (1:50, cat. number ab41489, Abcam), goat kif5b (1:500, cat. Number MBS420641, MyBioSource) and rabbit TOM20 (1:1000, cat. number ab186735, Abcam). After washing with PBS, the secondary antibodies were applied (1h, RT). For STED microscopy the following secondary antibodies were used: rabbit-Alexa594 (Invitrogen, 561 excitation) chicken-STAR635P (Abberior, 640 nm excitation), rat-Alexa488 (Invitrogen, 488 excitation), goat-STARRED (Abberior, 640 nm excitation). All antibodies were diluted in blocking medium. Three 10 min wash steps with PBS were performed and excess PBS was removed. All preparations were mounted in Citifluor (Citifluor Ltd.) or Mowiol (Merck) before imaging. For GTP-tubulin staining, we followed the protocol of Dimitrov *et al*. (15). Briefly, cells were treated with 0.05% Triton in GPEM

buffer (3 min, 37°C) before incubation with MB11 (1:250, cat. number AG-27B-0009-C100 Adipogen) diluted in GPEM buffer supplemented with 2% BSA (15 min, 37°C). After a quick wash in GPEM buffer, donkey anti human Alexa 594 (1:1000, cat. number 709-585-149, Jackson ImmunoResearch) was applied (15 min, 37°C) followed by methanol fixation. A Zeiss LSM 780 confocal laser scanning microscope (Zeiss) was used to record fluorescence images.

**Stimulated emission depletion (STED) microscopy & colocalisation analysis**

An Abberior Expert-Line STED (Abberior Instruments) microscope consisting of an inverted Olympus IX83 microscope body fitted with four pulsed (40 MHz) excitation laser modules (405, 485, 561 and 640 nm), two depletion beams at 595 and 775 nm, a motorized stage with P-736 PINano (Physik Instrumente) and the IX3-ZDC-12 z-drift compensation unit (Olympus) was used for multicolor STED imaging. To relocate cells a 20x Olympus Plan N 0.4 NA air objective was used while a 100x Olympus UPlanSApo 1.4 NA oil-immersion objective was used for STED recordings. Emission was detected using a spectral detection module and four avalanche photodiode detectors. For live-cell STED imaging, tubulin was stained with the far-red emitting dye Silicon rhodamine (SiR) using the SiR-tubulin Kit (0.5 µM, 10 min incubation, CY-SC002, Spirochrome) and imaged using 640 nm excitation and 775 nm depletion. Mitochondria were stained with Mitotracker green (75 nM, 10 min incubation, Thermo Fisher Scientific) and imaged in confocal mode using 488 nm excitation. Two-color STED imaging on fixed samples was performed using 775 nm depletion, three-color STED imaging using 775 nm and 595 nm depletion sequentially. In the 2D live-cell imaging configuration, in which a 2D STED XY doughnut was applied, we sampled using 25 x 25 nm pixels. For STED recordings in fixed samples, as used to determine whether mitochondria were within or at the rim of the microtubule bundle, a 3D STED volume (XY doughnut + Z) was applied and 40 x 40 x 50 nm voxels were used to sample the 3D image stacks. STED recordings were deconvolved using a theoretical point spread function based on the optical properties of the imaging system and stabilized using Huygens (SVI). To calculate interface percentages between mitochondria and microtubules, Imaris (Bitplane) surface rendering and the surface-to-surface colocalisation Xtension (Bitplane, Matthew Gastinger) were used. To quantify the amount of kinesin dots in proximity of the mitochondrial surface area or interface area between mitochondria and tubulin, kinesin dots were first localized using the ‘spot detection tool’. Consecutively, the spot to surface Xtension was used to quantify the amount of kinesin motors on aforementioned surface areas.

**Total internal reflection (TIRF) microscopy & kinesin velocity analysis**

GFP-tagged kinesin motors were recorded using a Zeiss Elyra PS1 (Zeiss) microscope with temperature control for activity recordings at 37°C. A 488 CW laser was used for excitation in combination with a Plan Apochromat 100x 1.46 NA Oil objective and CCD camera (Andor iXon DU-897 512x512). Kymographs were produced using the KymographBuilder plugin (Hadrien Mary, ImageJ) and stationary motors were removed by filtering in the frequency domain as shown in

Supplementary Figure 4. Velocities were calculated using the Directionality plugin (ImageJ) written by Jean-Yves Tinevez (60).

**Drosophila stocks and pharmacological treatment**

All flies were kept on standard corn meal and sugar cane syrup at 25°C. Fly stocks used: w[1118]; P{y[+t7.7] w[+mC]=GMR57C10-GAL4}attP2 obtained from BDSC and y[*] w[*]; P{w[+mC]=UAS-tdTomato.mito}2 obtained from Kyoto stock center. For pharmacological treatment, flies of the appropriate genotype were collected within 8 hours from eclosion and kept on petri dishes with 20% sucrose and 1% agarose for 3 hours at 25°C. Starved flies were then moved to tubes with standard corn meal and sugar cane syrup supplemented with taxol (10 nM, 100 nM, 1 µM or 10 µM, Paclitaxel Cytoskeleton Inc.) or DMSO (0.01%, Cytoskeleton Inc.). Recordings of mitochondrial transport were performed after 24-28 or 48-52 hours of continuous drug exposure.

**Spinning disk *in vivo* mitochondrial transport recording & analysis**

Flies were mounted in oil (refractive index 1.334, Zeiss Immersol) between glass coverslips spaced with double-sided tape as shown in Figure 6C and described previously (61). Mitochondrial transport recordings were performed on an inverted spinning disk microscope (Nikon Ti- Andor Revolution – Yogokawa CSU-X1 Spinning Disk) fitted with a Nikon 60x objective (Plan Apo, NA 1.27, W) and incubation chamber (Okolab, 25°C). TdTomato was excited with 561 nm laser light and a dual-band bandpass filter was used for emission (FF01-512/630-25, Laser 2000). The 10-minute long transport recordings consisted of 10 µm thick stacks, to account for wing movement, taken every 2 seconds. Mitochondrial time lapse recordings were registered using the StackReg plugin (ImageJ) and in-house Igor pro code was used to generate kymographs and analyze mitochondrial transport time lapse recordings as described previously (35, 62, 63).

**Statistics**

Graphpad Prism was used for statistical analysis: $p < 0.05$ (*), $p < 0.01$ (**), $p < 0.001$ (***) and bar graphs represent mean values with standard error of the mean. Shapiro-Wilk normality tests were used to assess the normal distribution of the data. To compare two groups, in case of a normal distribution, unpaired t-tests were conducted as a two-sided test, otherwise the Mann Whitney test was performed. To compare multiple groups, a two-way ANOVA was performed with multiple testing correction.

**Acknowledgments:** We would like to thank M. Moons for technical support and all current and past LENS members for scientific comments on the project, specifically An-Sofie Desmet and Tom Venneman for scientific discussions. We thank Prof. J. Hendrix and Dr. S. Duwé for assistance with TIRF recordings at the Dynamic Bioimaging Lab (BIOMED, UHasselt). We finally thank Prof. P.

Agostinis for use of the Seahorse analyzer and Prof. L. Kapitein (Utrecht) for the optogenetic constructs.

## References


1. MacAskill AF, Kittler JT. Control of mitochondrial transport and localization in neurons. Trends Cell Biol. 2010;20(2):102-12.
2. Lodish H BA, Zipursky SL, et al. Molecular Cell Biology. 4th edition ed. New York: W. H. Freeman; 2000.
3. Nicholls DG. Mitochondrial dysfunction and glutamate excitotoxicity studied in primary neuronal cultures. Curr Mol Med. 2004;4(2):149-77.
4. Kapitein LC, Hoogenraad CC. Which way to go? Cytoskeletal organization and polarized transport in neurons. Mol Cell Neurosci. 2011;46(1):9-20.
5. Misgeld T, Schwarz TL. Mitostasis in Neurons: Maintaining Mitochondria in an Extended Cellular Architecture. Neuron. 2017;96(3):651-66.
6. Grafstein B, Forman DS. Intracellular transport in neurons. Physiol Rev. 1980;60(4):1167-283.
7. Bartlett WP, Banker GA. An electron microscopic study of the development of axons and dendrites by hippocampal neurons in culture. I. Cells which develop without intercellular contacts. J Neurosci. 1984;4(8):1944-53.
8. Sheng ZH, Cai Q. Mitochondrial transport in neurons: impact on synaptic homeostasis and neurodegeneration. Nat Rev Neurosci. 2012;13(2):77-93.
9. Granatiero V, Manfredi G. Mitochondrial Transport and Turnover in the Pathogenesis of Amyotrophic Lateral Sclerosis. Biology (Basel). 2019;8(2).
10. Flannery PJ, Trushina E. Mitochondrial dynamics and transport in Alzheimer's disease. Mol Cell Neurosci. 2019;98:109-20.
11. Kneussel M, Wagner W. Myosin motors at neuronal synapses: drivers of membrane transport and actin dynamics. Nat Rev Neurosci. 2013;14(4):233-47.
12. Wilson L, Jordan MA. Microtubule dynamics: taking aim at a moving target. Chem Biol. 1995;2(9):569-73.
13. Ayoub AT, Craddock TJ, Klobukowski M, Tuszynski J. Analysis of the strength of interfacial hydrogen bonds between tubulin dimers using quantum theory of atoms in molecules. Biophys J. 2014;107(3):740-50.
14. Howard J, Hyman AA. Dynamics and mechanics of the microtubule plus end. Nature. 2003;422(6933):753-8.
15. Dimitrov A, Quesnoit M, Moutel S, Cantaloube I, Poüs C, Perez F. Detection of GTP-tubulin conformation in vivo reveals a role for GTP remnants in microtubule rescues. Science. 2008;322(5906):1353-6.
16. Aumeier C, Schaedel L, Gaillard J, John K, Blanchoin L, Théry M. Self-repair promotes microtubule rescue. Nat Cell Biol. 2016;18(10):1054-64.
17. Nakata T, Niwa S, Okada Y, Perez F, Hirokawa N. Preferential binding of a kinesin-1 motor to GTP-tubulin-rich microtubules underlies polarized vesicle transport. J Cell Biol. 2011;194(2):245-55.
18. Tropini C, Roth EA, Zanic M, Gardner MK, Howard J. Islands containing slowly hydrolyzable GTP analogs promote microtubule rescues. PLoS One. 2012;7(1):e30103.
19. Cassimeris L. Microtubule assembly: lattice GTP to the rescue. Curr Biol. 2009;19(4):R174-6.
20. Vemu A, Szczesna E, Zehr EA, Spector JO, Grigorieff N, Deaconescu AM, et al. Severing enzymes amplify microtubule arrays through lattice GTP-tubulin incorporation. Science. 2018;361(6404).
21. Schaedel L, John K, Gaillard J, Nachury MV, Blanchoin L, Théry M. Microtubules self-repair in response to mechanical stress. Nat Mater. 2015;14(11):1156-63.
22. Farías GG, Guardia CM, Britt DJ, Guo X, Bonifacino JS. Sorting of Dendritic and Axonal Vesicles at the Pre-axonal Exclusion Zone. Cell Rep. 2015;13(6):1221-32.
23. Kramer T, Greco TM, Taylor MP, Ambrosini AE, Cristea IM, Enquist LW. Kinesin-3 mediates axonal sorting and directional transport of alphaherpesvirus particles in neurons. Cell Host Microbe. 2012;12(6):806-14.

24. Guedes-Dias P, Nirschl JJ, Abreu N, Tokito MK, Janke C, Magiera MM, et al. Kinesin-3 Responds to Local Microtubule Dynamics to Target Synaptic Cargo Delivery to the Presynapse. Curr Biol. 2019;29(2):268-82.e8.
25. Shima T, Morikawa M, Kaneshiro J, Kambara T, Kamimura S, Yagi T, et al. Kinesin-binding-triggered conformation switching of microtubules contributes to polarized transport. J Cell Biol. 2018;217(12):4164-83.
26. Vale RD, Coppin CM, Malik F, Kull FJ, Milligan RA. Tubulin GTP hydrolysis influences the structure, mechanical properties, and kinesin-driven transport of microtubules. J Biol Chem. 1994;269(38):23769-75.
27. Xiao H, Verdier-Pinard P, Fernandez-Fuentes N, Burd B, Angeletti R, Fiser A, et al. Insights into the mechanism of microtubule stabilization by Taxol. Proc Natl Acad Sci U S A. 2006;103(27):10166-73.
28. Alushin GM, Lander GC, Kellogg EH, Zhang R, Baker D, Nogales E. High-resolution microtubule structures reveal the structural transitions in αβ-tubulin upon GTP hydrolysis. Cell. 2014;157(5):1117-29.
29. Rai A, Liu T, Glauser S, Katrukha EA, Estévez-Gallego J, Rodríguez-García R, et al. Taxanes convert regions of perturbed microtubule growth into rescue sites. Nat Mater. 2019.
30. Zhang R, Alushin GM, Brown A, Nogales E. Mechanistic Origin of Microtubule Dynamic Instability and Its Modulation by EB Proteins. Cell. 2015;162(4):849-59.
31. Iżycki D, Niezgoda AA, Kaźmierczak M, Piorunek T, Iżycka N, Karaszewska B, et al. Chemotherapy-induced peripheral neuropathy - diagnosis, evolution and treatment. Ginekol Pol. 2016;87(7):516-21.
32. Scripture CD, Figg WD, Sparreboom A. Peripheral neuropathy induced by paclitaxel: recent insights and future perspectives. Curr Neuropharmacol. 2006;4(2):165-72.
33. Kuroi K, Shimozuma K. Neurotoxicity of taxanes: symptoms and quality of life assessment. Breast Cancer. 2004;11(1):92-9.
34. Jordan MA, Toso RJ, Thrower D, Wilson L. Mechanism of mitotic block and inhibition of cell proliferation by taxol at low concentrations. Proc Natl Acad Sci U S A. 1993;90(20):9552-6.
35. Van Steenbergen V, Boesmans W, Li Z, de Coene Y, Vints K, Baatsen P, et al. Molecular understanding of label-free second harmonic imaging of microtubules. Nat Commun. 2019;10(1):3530.
36. Elie-Caille C, Severin F, Helenius J, Howard J, Muller DJ, Hyman AA. Straight GDP-tubulin protofilaments form in the presence of taxol. Curr Biol. 2007;17(20):1765-70.
37. van Bergeijk P, Adrian M, Hoogenraad CC, Kapitein LC. Optogenetic control of organelle transport and positioning. Nature. 2015;518(7537):111-4.
38. Cai Q, Sheng ZH. Mitochondrial transport and docking in axons. Exp Neurol. 2009;218(2):257-67.
39. Hollenbeck PJ, Saxton WM. The axonal transport of mitochondria. J Cell Sci. 2005;118(Pt 23):5411-9.
40. Schon EA, Przedborski S. Mitochondria: the next (neurode)generation. Neuron. 2011;70(6):1033-53.
41. Chen H, Chan DC. Mitochondrial dynamics--fusion, fission, movement, and mitophagy--in neurodegenerative diseases. Hum Mol Genet. 2009;18(R2):R169-76.
42. Stowers RS, Megeath LJ, Górska-Andrzejak J, Meinertzhagen IA, Schwarz TL. Axonal transport of mitochondria to synapses depends on milton, a novel Drosophila protein. Neuron. 2002;36(6):1063-77.
43. Glater EE, Megeath LJ, Stowers RS, Schwarz TL. Axonal transport of mitochondria requires milton to recruit kinesin heavy chain and is light chain independent. J Cell Biol. 2006;173(4):545-57.
44. Wang X, Schwarz TL. The mechanism of Ca2+ -dependent regulation of kinesin-mediated mitochondrial motility. Cell. 2009;136(1):163-74.
45. Liu X, Hajnóczky G. Ca2+-dependent regulation of mitochondrial dynamics by the Miro-Milton complex. Int J Biochem Cell Biol. 2009;41(10):1972-6.

46. Peet DR, Burroughs NJ, Cross RA. Kinesin expands and stabilizes the GDP-microtubule lattice. Nat Nanotechnol. 2018;13(5):386-91.
47. Arnal I, Wade RH. How does taxol stabilize microtubules? Curr Biol. 1995;5(8):900-8.
48. Ross JL, Shuman H, Holzbaur EL, Goldman YE. Kinesin and dynein-dynactin at intersecting microtubules: motor density affects dynein function. Biophys J. 2008;94(8):3115-25.
49. Conway L, Gramlich MW, Ali Tabei SM, Ross JL. Microtubule orientation and spacing within bundles is critical for long-range kinesin-1 motility. Cytoskeleton (Hoboken). 2014;71(11):595-610.
50. Dixit R, Ross JL, Goldman YE, Holzbaur EL. Differential regulation of dynein and kinesin motor proteins by tau. Science. 2008;319(5866):1086-9.
51. Hoeprich GJ, Thompson AR, McVicker DP, Hancock WO, Berger CL. Kinesin's neck-linker determines its ability to navigate obstacles on the microtubule surface. Biophys J. 2014;106(8):1691-700.
52. Bálint Š, Verdeny Vilanova I, Sandoval Álvarez Á, Lakadamyali M. Correlative live-cell and superresolution microscopy reveals cargo transport dynamics at microtubule intersections. Proc Natl Acad Sci U S A. 2013;110(9):3375-80.
53. LaPointe NE, Morfini G, Brady ST, Feinstein SC, Wilson L, Jordan MA. Effects of eribulin, vincristine, paclitaxel and ixabepilone on fast axonal transport and kinesin-1 driven microtubule gliding: implications for chemotherapy-induced peripheral neuropathy. Neurotoxicology. 2013;37:231-9.
54. Li Q, King SJ, Xu J. Native kinesin-1 does not bind preferentially to GTP-tubulin-rich microtubules in vitro. Cytoskeleton (Hoboken). 2017;74(9):356-66.
55. Bhattacharya MR, Gerdts J, Naylor SA, Royse EX, Ebstein SY, Sasaki Y, et al. A model of toxic neuropathy in Drosophila reveals a role for MORN4 in promoting axonal degeneration. J Neurosci. 2012;32(15):5054-61.
56. Hamoudi Z, Khuong TM, Cole T, Neely GG. A fruit fly model for studying paclitaxel-induced peripheral neuropathy and hyperalgesia. F1000Res. 2018;7:99.
57. Vagnoni A, Bullock SL. A cAMP/PKA/Kinesin-1 Axis Promotes the Axonal Transport of Mitochondria in Aging Drosophila Neurons. Curr Biol. 2018;28(8):1265-72.e4.
58. Theiss C, Meller K. Taxol impairs anterograde axonal transport of microinjected horseradish peroxidase in dorsal root ganglia neurons in vitro. Cell Tissue Res. 2000;299(2):213-24.
59. Lavoie-Cardinal F, Salesse C, Bergeron É, Meunier M, De Koninck P. Gold nanoparticle-assisted all optical localized stimulation and monitoring of $Ca^{2+}$ signaling in neurons. Sci Rep. 2016;6:20619.
60. Liu ZQ. Scale space approach to directional analysis of images. Appl Opt. 1991;30(11):1369-73.
61. Vagnoni A, Bullock SL. A simple method for imaging axonal transport in aging neurons using the adult Drosophila wing. Nat Protoc. 2016;11(9):1711-23.
62. Boesmans W, Ameloot K, van den Abbeel V, Tack J, Vanden Berghe P. Cannabinoid receptor 1 signalling dampens activity and mitochondrial transport in networks of enteric neurones. Neurogastroenterol Motil. 2009;21(9):958-e77.
63. Vanden Berghe P. Fluorescent molecules as tools to study Ca2+ signaling, mitochondrial dynamics and synaptic function in enteric neurons. Verh K Acad Geneeskd Belg. 2004;66(5-6):407-25.

## Figures

**Figure 1. Mitochondrial transport patterns correlate and are influenced by the molecular conformation of tubulin dimers.**

(A). Immunohistochemical staining of α-tubulin (yellow), GTP-bound tubulin dimers (magenta) and MAP2 (cyan) in hippocampal cultures at 7 DIV. (B) Quantification of the staining intensity of α-tubulin (20.7±9.2 vs. 32.8±18, n=27 cells from 3 independent experiments; * $p<0.05$ Mann Whitney test), GTP-bound tubulin (34.3±12.8 vs. 35.3±18, n=27 cells from 3 independent experiments; Unpaired two-tailed t-test) and their ratio (1.8±0.5 vs. 1.2±0.4, n=27 cells from 3 independent experiments; *** $p<0.001$ Unpaired two-tailed t-test) in either axonal or dendritic processes. (C) Hippocampal neuron loaded with mitotracker red to visualize mitochondria and (D) kymographs of axonal and dendritic projections. (E) A negative correlation was found between anterograde transport velocities and the amount of tubulin dimers in a GTP-bound conformation (n=42 neuronal processes from 3 independent experiments: ** $p<0.01$ Spearman correlation (-0.41), scatterplot ± 95% confidence interval) but not between retrograde velocities and GTP-tubulin density. (F) Hippocampal neurons transfected with TOM20-mCherry, incubated with DMSO (Control) or taxol (4h, 10 nM), red arrows indicate axonal processes used for analysis. (G) Quantification of the number of motile mitochondria per 100 micrometer axon shows a significant reduction in anterograde mitochondria in taxol-treated cells compared to control axons (1.7±1.3 vs. 0.7±0.8, n=27 neurons from 3 independent experiments; ** $p<0.01$ Mann Whitney test) but not a loss of retrograde moving mitochondria (1.5±1.2 vs. 1.2±0.7, n=27 neurons from 3 independent experiments; Unpaired Welch two-tailed t-test). (H) Although fewer motile mitochondria were present, a significant increase in anterograde (0.26±0.1 vs. 0.38±0.2) but not retrograde (0.32±0.15 vs. 0.30±0.1), velocities in taxol-treated cells was observed (n=22 neurons from 3 independent experiments; ** $p<0.01$ Mann Whitney test). Indicated values are mean ± standard deviation, bar plots represent mean with standard error of the mean.

**Figure 2. Mitochondria are transported along and within the microtubule bundle**

(A) Live two-color 2D STED time lapse recordings of hippocampal neurons loaded with mitotracker green (mitochondria, yellow) and SiR Tubulin (microtubules, cyan). A line profile perpendicular to the direction of transport (arrowheads) of a motile mitochondrion (arrows) is shown with the corresponding intensity profile for the tubulin (cyan plot and overlaid Gaussians) and mitochondrion (yellow and overlaid Gaussian) signal. The mitochondrion left in the image is clearly positioned at the rim, while the mitochondrion indicated by the arrows could be within the microtubule bundle. (B) Graphical overview of the different steps required to assess the nano-position of mitochondria during mitochondrial transport. Mitotracker-labelled hippocampal neurons were used for live imaging and axonal processes were selected based on process length and diameter. Upon detection of motile mitochondria paraformaldehyde (PFA) was added during the live recording followed by IHC processing and finally relocalisation of the motile mitochondria for high resolution 3D STED recordings. (C) Mitotracker red was loaded onto hippocampal neurons before mitochondrial transport recordings. Paraformaldehyde was added during recordings to halt mitochondrial transport and all other intracellular processes.

Kymograph indicating an anterogradely moving mitochondrion as seen moving in panels (arrows). (D) After immunohistochemical staining (TOM20 and ß-tubulin), (E) z-stacks were recorded using 3D STED, deconvolved in SVI and rendered in Imaris. (F) Cross-section of the mitochondrion and microtubules. (G) Surface rendering of mitochondria and tubulin was performed followed by (H) calculation of the surface$^{MITO-MT}$ overlap (51.5±15.4%, n=44 mitochondria from 3 independent experiments, mean with standard error of the mean).

**Figure 3. Excess of elongated tubulin dimers hinders mitochondrial transport within the microtubule bundle**

(A) Hippocampal neurons were loaded with mitotracker after incubation with DMSO as control or (B) taxol (10nM, 4h) and axons were selected based on process length and diameter. During transport recordings, paraformaldehyde was added to the imaging buffer at the moment an anterograde motile mitochondrion was observed (arrows). After fixation and immunohistochemical staining using antibodies for β-tubulin and TOM20, z-stacks were recorded using STED microscopy, deconvolved and surface rendered to calculate the surface$^{MITO-MT}$ overlap percentage. (C) The surface$^{MITO-MT}$ overlap did not differ between control (52.6±23.7%) and taxol-treated neurons (53.5±28.4%) in case all mitochondria (moving and stationary) were considered (n=264 mitochondria from 3 independent experiments; Mann Whitney test), but (D) was significantly lower in taxol versus control (38.6±14.7% vs 51.5.6±15.4%) when only motile mitochondria were considered in the comparison (n=39 mitochondria from 3 independent experiments; *** p<0.001 Mann Whitney test). Indicated values are mean ± standard deviation, bar plots represent mean with standard error of the mean. (E) Graphical overview of motile mitochondria at the rim and within the microtubule bundle in control axons while only mitochondria at the rim are transported in axonal processes after taxol incubation.

**Figure 4. Elongated tubulin dimers increase Kif5B velocity and localize at the microtubule-mitochondrial interface**

(A) TIRF microscopy of hippocampal neurons transfected with Kif5b-eGFP constructs, arrows indicate motile kinesin motors. (B) Frequency distribution of KIF5B velocities in DMSO (control) or taxol-treated samples (10 nM, 4h) shows increased velocities in taxol-treated cells (n=27 neuronal fibers from 3 independent experiments; ** p<0.01 Gaussian Least squares fit). (C) Hippocampal neurons loaded with mitotracker after incubation with DMSO as control or taxol (10nM, 4h). During transport recordings, paraformaldehyde was added at the moment an anterograde motile mitochondrion was observed (arrows). (D) 2D STED microscopy was used to record Z-stacks on the fixed samples using antibodies for α-tubulin, TOM20 and KIF5B, image stacks were deconvolved in Huygens (SVI), rendered and analysed in Imaris. (E) Quantification reveals that the number KIF5B spots present on the surface of motile mitochondria (entire surface considered) does not differ between control (1.3±0.6) and taxol-treated axons (1.3±0.6, n=40 mitochondria from 3 independent experiments; Mann Whitney test). (F) Quantification of the KIF5B spots residing specifically in the surface$^{MITO-MT}$ overlap, shows an increase due to taxol-treatment (2.4±1.3 vs. 1.8±0.9 in control, n=40 mitochondria from 3 independent experiments; * p<0.05 Unpaired Welch two-tailed t-test). (G) Hippocampal neurons were

transfected with two constructs: TOM20-mCherry-LOV and Kif5b-GFP-ePDZb1. Upon illumination with blue light, the Light-Oxygen-Voltage (LOV)-domain and ePDZ1 domain heterodimerize, forcing a link between kinesin motors (KIF5B) and mitochondria (TOM20). Axonal processes were selected based on process length and diameter. (H) Examples of kymographs before and after illumination, indicated by the red dotted line in the kymograph. (I) Quantification of the percentage of motile anterograde mitochondria between the dark and illuminated condition in control and taxol cells, and the control and taxol condition in illuminated (LIGHT) state. (J) Quantification of the anterograde transport velocity between the dark and illuminated condition in control and taxol cells, and between the control and taxol condition in illuminated (LIGHT) state. Indicated values are mean ± standard deviation, bar plots represent mean with standard error of the mean.

**Figure 5. Taxol halts the majority of mitochondrial transport in the anterograde direction while increasing anterograde transport velocities in *vivo***

(A) *UAS-mito::tdTomato*/+; *Nsyb-Gal4/+* virgins were selected for pharmacological treatment within 8 hours from eclosion. After a 3-hour starvation period, flies were transferred to food vials containing regular food supplemented with DMSO as control or taxol (100 nM) for 24 or 48 hours before imaging. (B) Axonal projections and neuronal cell bodies were visible along the L1 and L2 veins in the wing, the branching region in L2 was used for transport recordings to reduce the number of axons and facilitate analysis. (C) Flies were mounted between two coverslips using double-sided tape and mitochondrial transport recorded using an inverted spinning disk microscope. (D) Sum projection of a mitochondrial time lapse recording and corresponding kymograph. (E) Quantification of the number of motile anterograde mitochondria per 100 micrometer shows a significant reduction in motile mitochondria in taxol (TXL)-treated flies compared to control neurons after 24h (16.6±5.7 vs. 11.1±4, n=19 flies from 3 independent experiments; ** $p<0.01$ Unpaired two-tailed t-test) and 48h (9.4±3.3 vs. 6.7±3.7, n=19 flies from 3 independent experiments; * $p<0.05$ Unpaired two-tailed t-test). The number of retrograde motile mitochondria remained unchanged after 24 h (9.1±4.4 vs. 8±3.2, n=19 flies from 3 independent experiments; * $p<0.05$ Unpaired two-tailed t-test) but significantly decreased after 48 hours taxol (6±2.3 vs. 4.2±2.8, n=19 flies from 3 independent experiments; * $p<0.05$ Unpaired two-tailed t-test). (F) Anterograde transport velocities were significantly increased after 24 h (0.19±0.03 vs. 0.22±0.03) and 48 h (0.17±0.06 vs. 0.20±0.05) taxol treatment while retrograde velocities remained unchanged compared to controls (24h: 0.25±0.06 vs. 0.27±0.06; 48h: 0.22±0.05 vs. 0.20±0.08, n=19 flies from 3 independent experiments; * $p<0.05$ Unpaired two-tailed t-test, for each condition). Indicated values are mean ± standard deviation, bar plots represent mean with standard error of the mean.

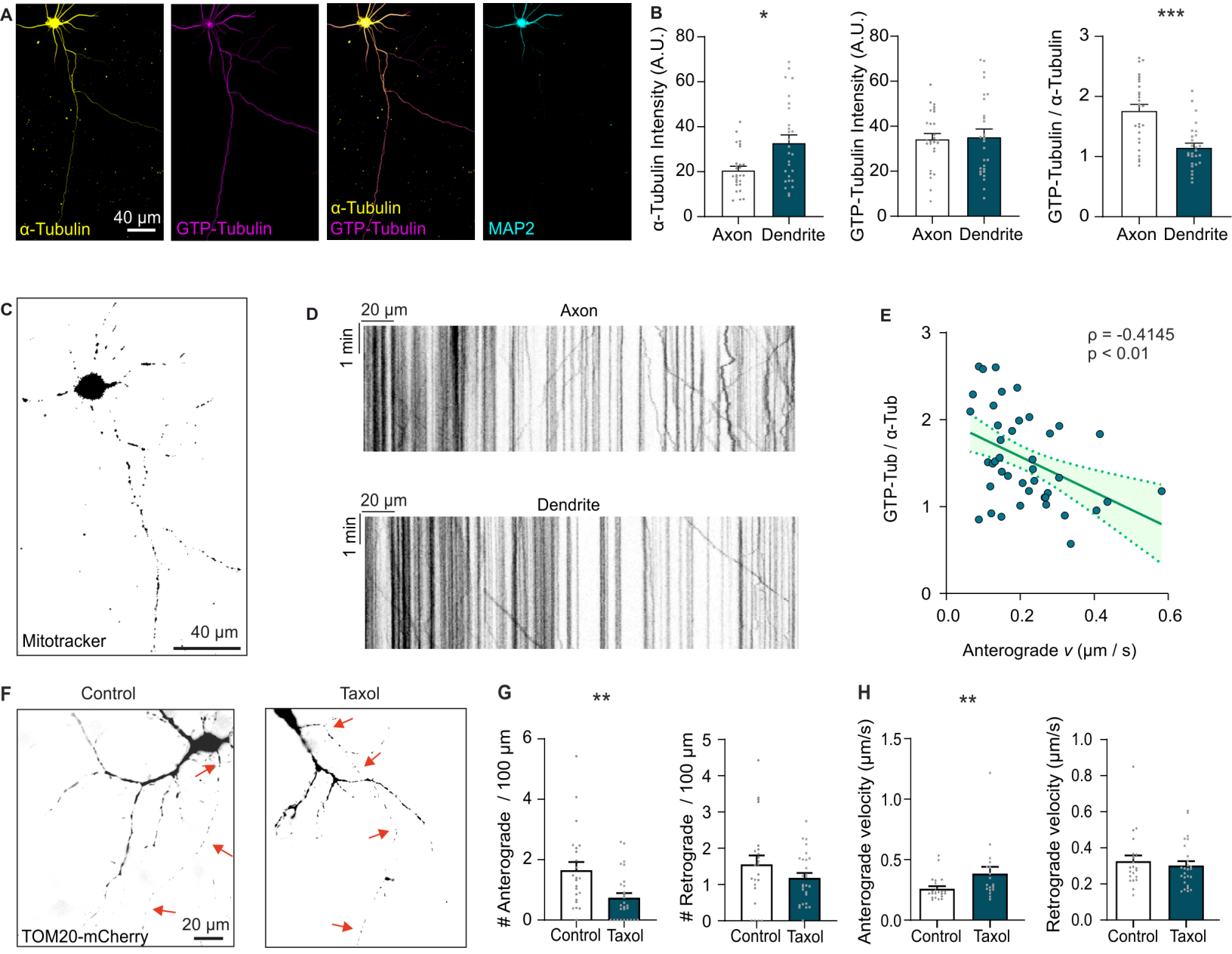
A
α-Tubulin
40 μm
GTP-Tubulin
α-Tubulin
GTP-Tubulin
MAP2
B
α-Tubulin Intensity (A.U.)
*
Axon Dendrite
GTP-Tubulin Intensity (A.U.)
Axon Dendrite
GTP-Tubulin / α-Tubulin
***
Axon Dendrite
C
Mitotracker
40 μm
D
20 μm
Axon
1 min
20 μm
Dendrite
1 min
E
ρ = -0.4145
p < 0.01
GTP-Tub / α-Tub
Anterograde v (μm / s)
F
Control
Taxol
TOM20-mCherry
20 μm
G
**
# Anterograde / 100 μm
Control Taxol
# Retrograde / 100 μm
Control Taxol
H
**
Anterograde velocity (μm/s)
Control Taxol
Retrograde velocity (μm/s)
Control Taxol

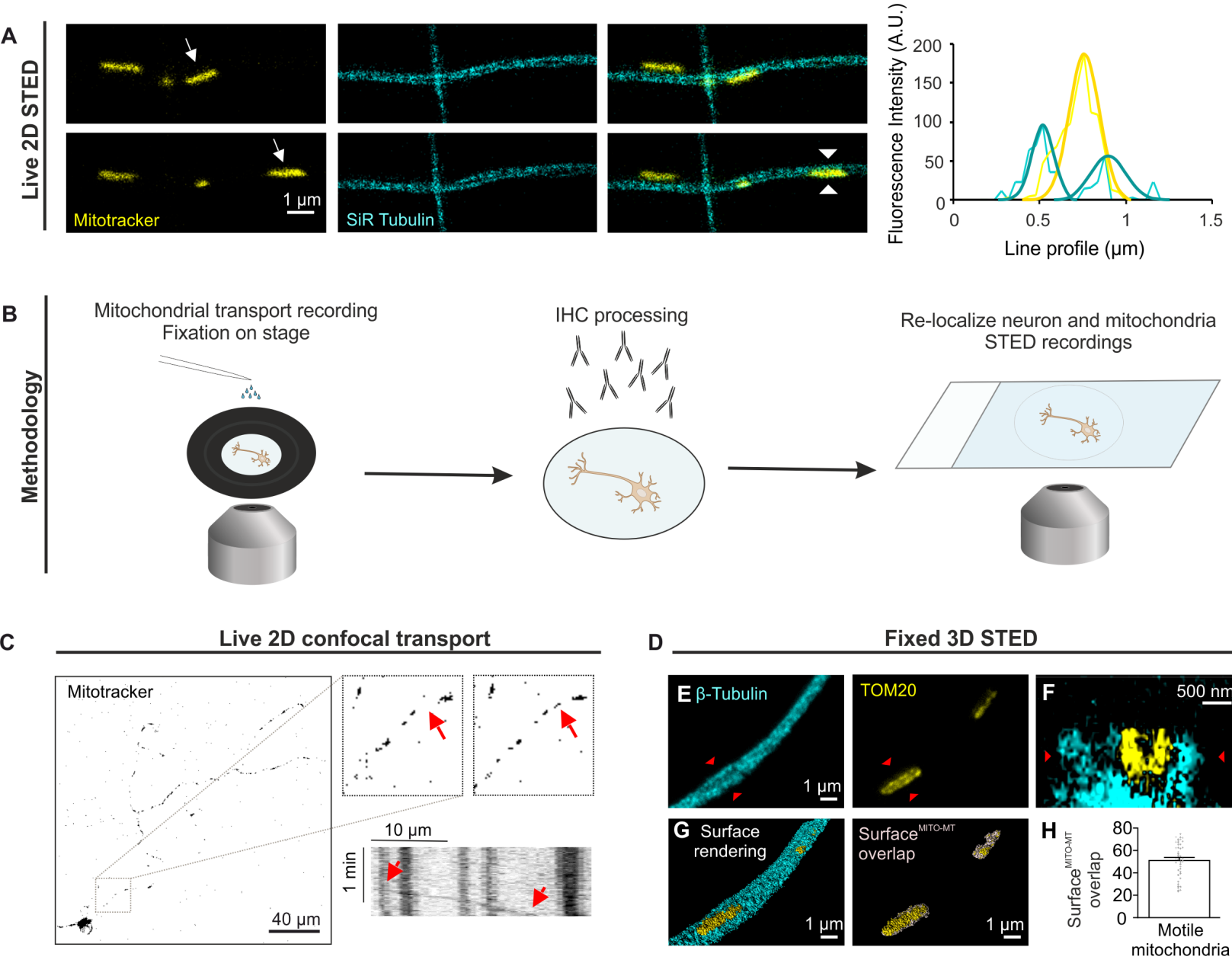
A
Live 2D STED
Mitotracker
1 µm
SiR Tubulin
Fluorescence Intensity (A.U.)
200
150
100
50
0
0
0.5
1
1.5
Line profile (µm)
B
Methodology
Mitochondrial transport recording
Fixation on stage
IHC processing
Re-localize neuron and mitochondria
STED recordings
C
Live 2D confocal transport
Mitotracker
40 µm
10 µm
1 min
D
Fixed 3D STED
E β-Tubulin
1 µm
TOM20
F
500 nm
G Surface
rendering
1 µm
Surface MITO-MT
overlap
1 µm
H
Surface MITO-MT overlap
80
60
40
20
0
Motile
mitochondria

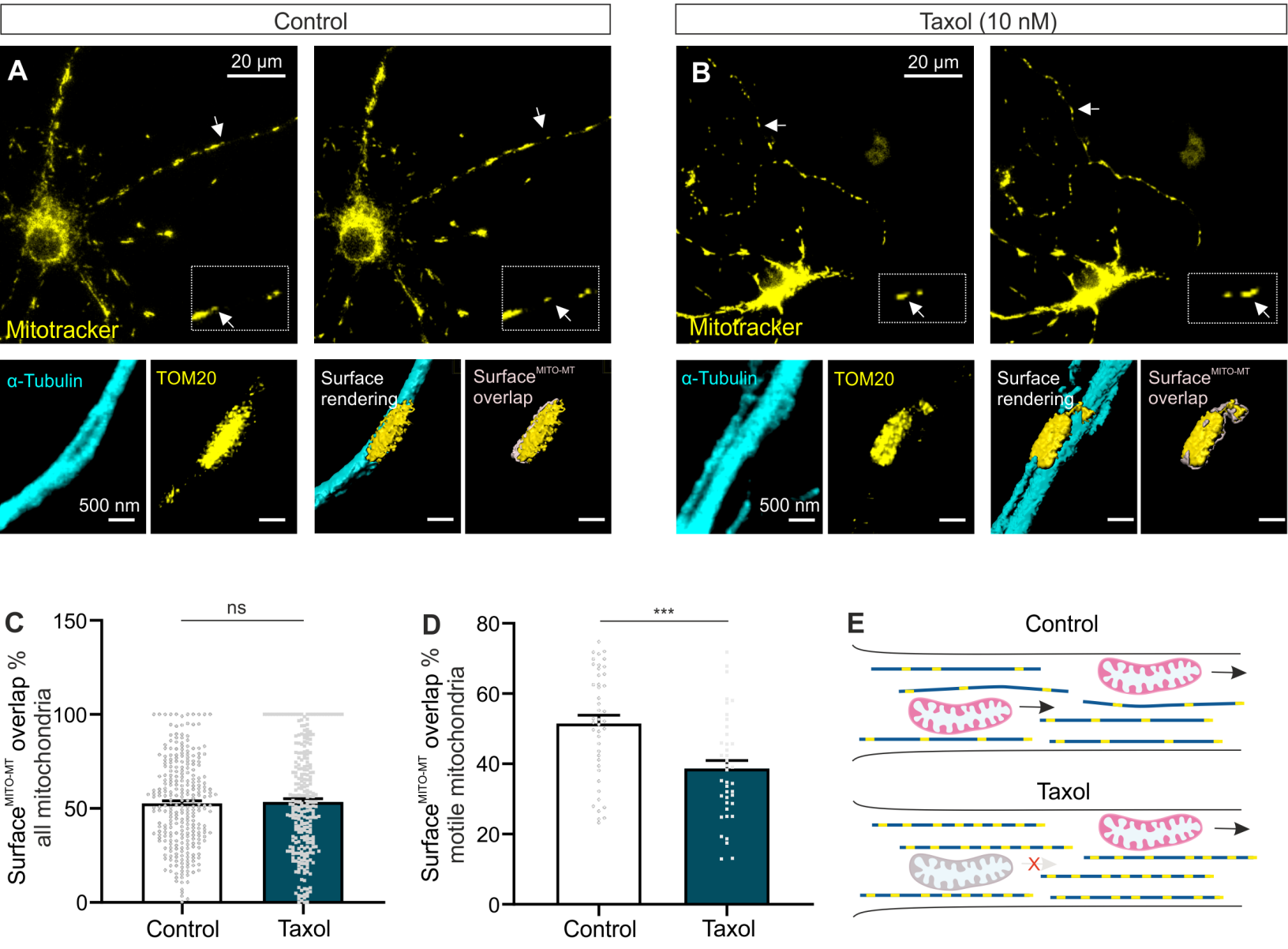
Control
Taxol (10 nM)
A
B
20 µm
Mitotracker
α-Tubulin
TOM20
Surface rendering
Surface MITO-MT overlap
500 nm
C
ns
Surface MITO-MT overlap % all mitochondria
150
100
50
0
Control
Taxol
D
***
Surface MITO-MT overlap % motile mitochondria
80
60
40
20
0
Control
Taxol
E
Control
Taxol
X

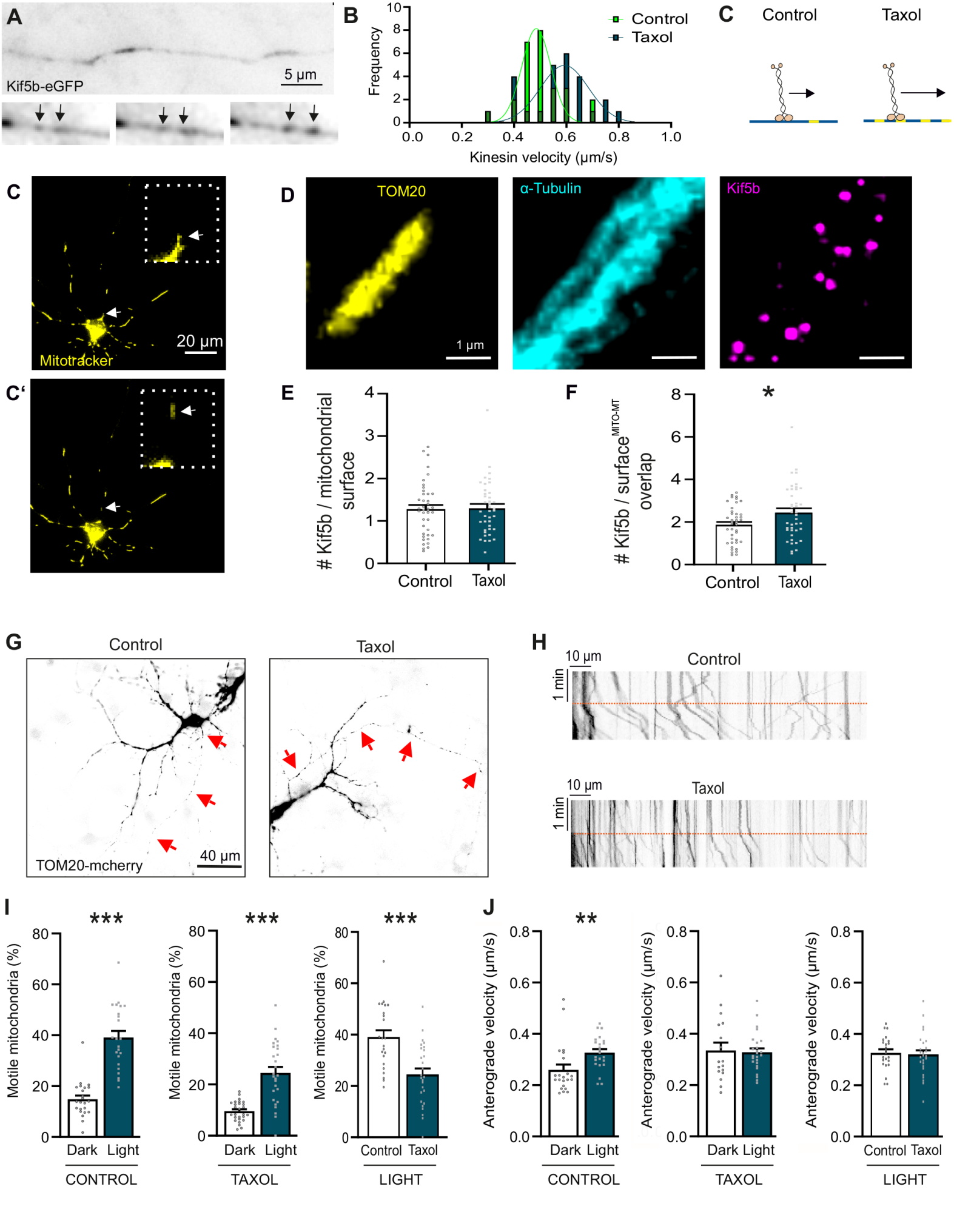
A
Kif5b-eGFP
5 µm
B
Frequency
Kinesin velocity (µm/s)
Control
Taxol
C
Control
Taxol
C
Mitotracker
20 µm
C'
D
TOM20
α-Tubulin
Kif5b
1 µm
E
# Kif5b / mitochondrial surface
Control
Taxol
F
# Kif5b / surface MITO-MT overlap
*
Control
Taxol
G
Control
Taxol
TOM20-mcherry
40 µm
H
10 µm
1 min
Control
Taxol
I
Motile mitochondria (%)
***
Dark Light
CONTROL
TAXOL
Control Taxol
LIGHT
J
Anterograde velocity (µm/s)
**
Dark Light
CONTROL
TAXOL
Control Taxol
LIGHT

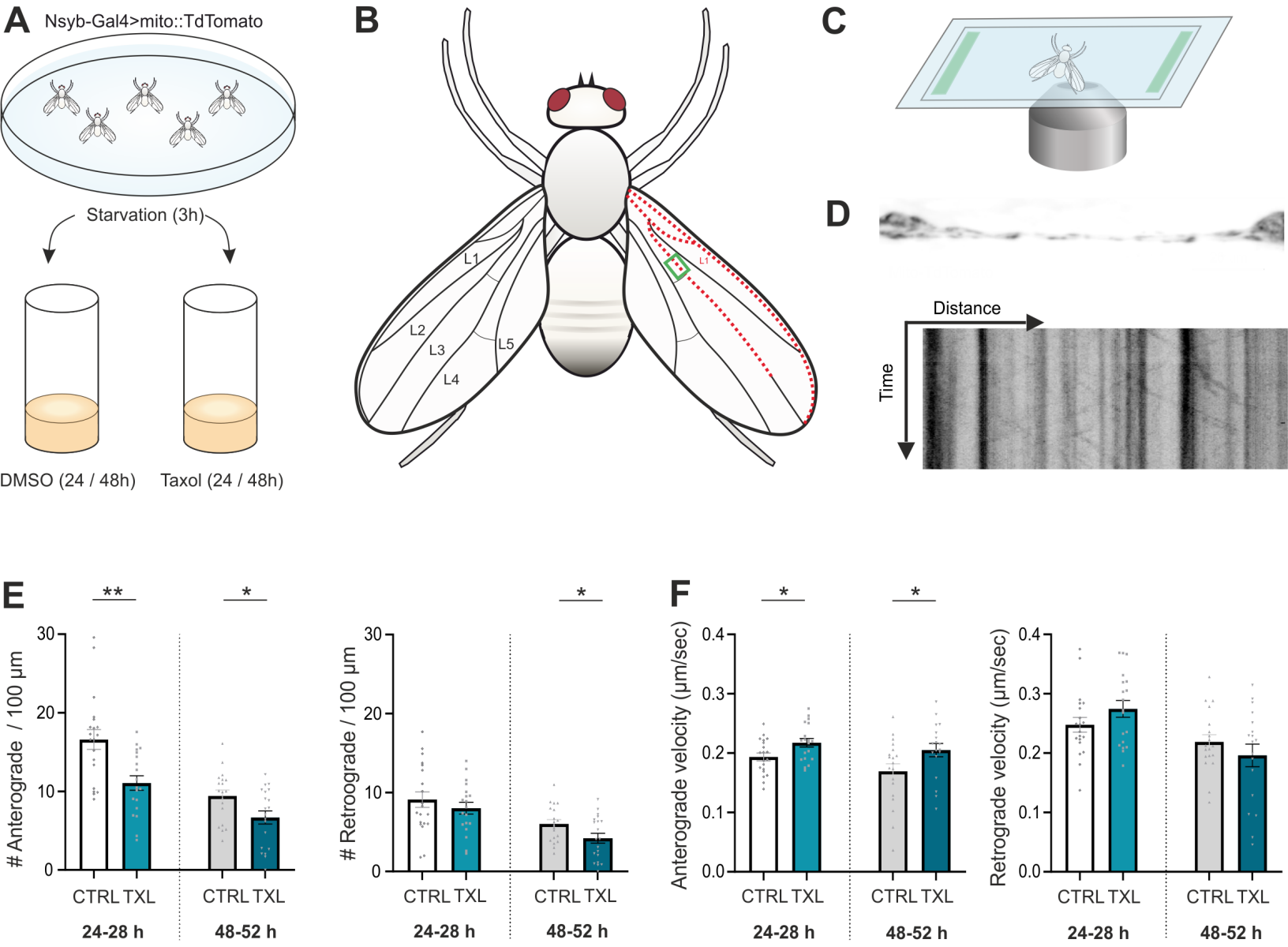
A
Nsyb-Gal4>mito::TdTomato
Starvation (3h)
DMSO (24 / 48h)
Taxol (24 / 48h)
B
L1
L2
L3
L4
L5
C
D
Distance
Time
E
# Anterograde / 100 µm
# Retroograde / 100 µm
CTRL TXL
24-28 h
48-52 h
F
Anterograde velocity (µm/sec)
Retrograde velocity (µm/sec)